Three-dimensional tracking of cardiac catheters using an inverse geometry x-ray fluoroscopy system

Michael A. Speidel[a)]
Department of Medical Physics, University of Wisconsin–Madison, Madison, Wisconsin 53705

Michael T. Tomkowiak
Department of Biomedical Engineering, University of Wisconsin–Madison, Madison, Wisconsin 53705

Amish N. Raval
Department of Medicine, University of Wisconsin–Madison, Madison, Wisconsin 53792

Michael S. Van Lysel
Department of Medicine and Department of Medical Physics, University of Wisconsin–Madison, Madison, Wisconsin 53792

(Received 22 June 2010; revised 21 October 2010; accepted for publication 23 October 2010; published 23 November 2010)

Purpose: Scanning beam digital x-ray (SBDX) is an inverse geometry fluoroscopic system with high dose efficiency and the ability to perform continuous real-time tomosynthesis at multiple planes. This study describes a tomosynthesis-based method for 3D tracking of high-contrast objects and present the first experimental investigation of cardiac catheter tracking using a prototype SBDX system.

Methods: The 3D tracking algorithm utilizes the stack of regularly spaced tomosynthetic planes that are generated by SBDX after each frame period (15 frames/s). Gradient-filtered versions of the image planes are generated, the filtered images are segmented into object regions, and then a 3D coordinate is calculated for each object region. Two phantom studies of tracking performance were conducted. In the first study, an ablation catheter in a chest phantom was imaged as it was pulled along a 3D trajectory defined by a catheter sheath (10, 25, and 50 mm/s pullback speeds). SBDX tip tracking coordinates were compared to the 3D trajectory of the sheath as determined from a CT scan of the phantom after the registration of the SBDX and CT coordinate systems. In the second study, frame-to-frame tracking precision was measured for six different catheter configurations as a function of image noise level (662–7625 photons/mm^2 mean detected x-ray fluence at isocenter).

Results: During catheter pullbacks, the 3D distance between the tracked catheter tip and the sheath centerline was 1.0 ± 0.8 mm (mean $\pm$one standard deviation). The electrode to centerline distances were comparable to the diameter of the catheter tip (2.3 mm), the confining sheath (4 mm outside diameter), and the estimated SBDX-to-CT registration error (± 0.7 mm). The tip position was localized for all 332 image frames analyzed and 83% of tracked positions were inside the 3D sheath volume derived from CT. The pullback speeds derived from the catheter trajectories were within 5% of the programed pullback speeds. The tracking precision of ablation and diagnostic catheter tips ranged from ± 0.2 mm at the highest image fluence to ± 0.9 mm at the lowest fluence. Tracking precision depended on image fluence, the size of the tracked catheter electrode, and the contrast of the electrode.

Conclusions: High speed multiplanar tomosynthesis with an inverse geometry x-ray fluoroscopy system enables 3D tracking of multiple high-contrast objects at the rate of fluoroscopic imaging. The SBDX system is capable of tracking electrodes in standard cardiac catheters with approximately 1 mm accuracy and precision. © *2010 American Association of Physicists in Medicine*.
[DOI: 10.1118/1.3515463]

Key words: catheter tracking, inverse geometry, fluoroscopy, tomosynthesis, image guidance

I. INTRODUCTION

Catheter ablation has become a widespread treatment for a range of cardiac arrhythmias, including forms of atrial fibrillation and ventricular tachycardia. In the traditional electrophysiology approach, a multielectrode catheter is guided inside the cardiac chambers under x-ray fluoroscopy. The endomyocardial surface is probed to create a map of electrical activation and then energy is delivered through the tip to destroy triggers or pathways of arrhythmia propagation. Recently, ablation strategies have been developed to electrically isolate cardiac anatomy that is critical to arrhythmia propagation. For example, in atrial fibrillation, there may be multiple trigger sites within the sleeves of atrial tissue extending into the pulmonary veins.[1] Instead of targeting all of these sites separately, operators ablate circumferentially around the pulmonary vein ostia[2] or antrum.[3] These anatomic ablation

strategies demand accurate real-time knowledge of catheter tip position relative to moving 3D cardiac structures.

Conventional x-ray fluoroscopy offers high resolution real-time imaging of metallic catheter electrodes. However, the lack of depth information and poor soft tissue contrast in a 2D x-ray projection limits the utility of fluoroscopy alone for anatomic-based ablation. Biplane x-ray fluoroscopy improves the ability to appreciate catheter position in 3D but the ionizing radiation dose to the patient is a source of concern. Radiofrequency catheter ablation (RFCA) is associated with long fluoroscopic imaging times and radiation-induced skin injuries have been reported.[4] A study of 28 RFCA procedures reported the fluoroscopic time from both planes averaged 120.8 min ($\pm$62.6 min), with peak skin dose increasing with both fluoroscopic time and patient weight.[5] The mean effective radiation dose from biplane fluoroscopy during ablation of atrial fibrillation has been reported as 15.2–39.0 mSv, increasing with body mass index.[6]

Nonfluoroscopic 3D electromagnetic (EM) catheter tracking systems have emerged as an important tool for catheter ablation. These systems perform 3D tip tracking using a local magnetic field emitter and a field-sensing catheter tip.[7] The tracked positions can be used to generate 3D electroanatomic maps of activation time and can be merged with preacquired volume images of cardiac anatomy (e.g., cardiac CT).[8] EM tracking facilitates catheter ablation but has several limitations. Specialized catheters and external equipment are required. Trackable catheters are limited to those offered by the tracking system vendor. The specialized hardware components built into the catheter constrain device profile and mechanical performance. Since these systems do not provide live imaging, they are typically used in combination with conventional x-ray fluoroscopy. Low dose imaging methods that could offer 3D localization and tracking of any catheter device would be an appealing alternative.

Inverse geometry x-ray fluoroscopy, based on scanning beam digital x-ray (SBDX) technology, has the potential to substantially reduce patient x-ray doses and also provide three-dimensional tracking of unmodified catheters by using real-time tomosynthesis.[9–12] SBDX performs fluoroscopy and angiography at 15–30 frames/s using a rapidly scanned narrow x-ray beam directed at a small-area photon-counting detector array (Fig. 1). As detailed in Ref. 10, the use of a narrow x-ray beam, distant detector, and thick CdTe x-ray detector results in low levels of detected scatter and high x-ray stopping efficiency over a range of kVps, which in turn allow a given image signal-to-noise ratio (SNR) to be achieved with lower x-ray output and lower patient dose. Inverse geometry spreads the source x-rays over a larger area at the patient entrance, further reducing skin dose. Signal-to-noise ratio and entrance exposure measurements on a prototype SBDX system have demonstrated the potential for 84% entrance exposure reduction without loss of SNR compared to a conventional cardiac angiographic system at equal kVp.[11]

The inverted system geometry also gives SBDX a unique real-time tomosynthesis capability. SBDX simultaneously reconstructs multiple tomosynthetic images spaced throughout the patient, each of which portrays in-plane objects in focus and out-of-plane objects as blurred. A 2D multiplane composite is generated for live display.[10] Recently, algorithms were described that use the tomosynthetic images generated by SBDX to perform 3D tracking of high-contrast objects such as catheter electrodes.[12] Computer simulations of simple geometric phantoms indicated 3D tracking with submillimeter accuracy and precision was feasible, depending on image SNR, object velocity, and system tomographic angle.

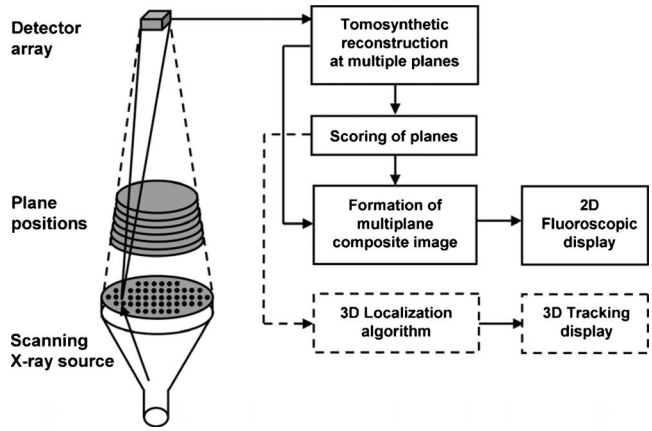

FIG. 1. The SBDX system uses a raster scanned focal spot, transmission target, multihole collimator, and hardware based reconstructor. Boxes with solid lines indicate the steps of image formation and image presentation in the current SBDX prototype. The proposed catheter tracking steps are shown with dashed lines.

In this paper, we present the first investigation of the SBDX catheter tracking algorithm using images acquired with an SBDX prototype. The catheter tracking algorithm is detailed and two phantom studies are reported. In the first study, the accuracy and precision of catheter tracking is evaluated in the presence of anatomic background for different catheter velocities. In the second study, the precision of 3D localization is determined for six different cardiac catheter geometries as a function of image SNR.

II. ALGORITHM

The 3D catheter tracking algorithm is an extension of the tomosynthetic image reconstruction and plane scoring technique that is used to generate the live multiplane composite display for SBDX. We begin with a brief review of the SBDX scanning and image reconstruction method and then describe the catheter tracking algorithm.

II.A. Scanning and image reconstruction

The SBDX x-ray source consists of a magnetically deflected focal spot, a planar transmission target, and a multihole collimator. The collimator holes define a set of narrow overlapping x-ray beams directed at the x-ray detector. There are 100×100 focal spot positions on a 2.3 mm pitch. The detector is located 1500 mm above the target plane in the x-ray source. The source and detector are mounted to a gan-

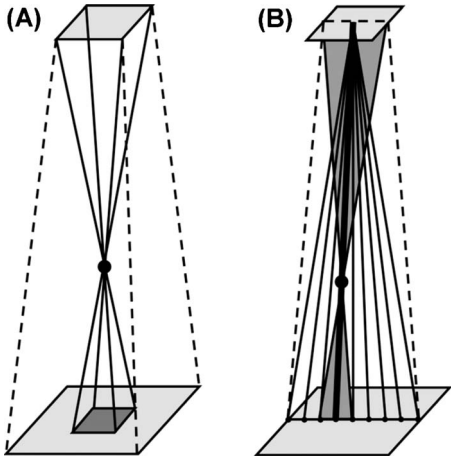

FIG. 2. SBDX tomographic blur. (a) A point in the patient is imaged by a patch of the source array, typically 10×10 spots. Backprojecting the point to planes away from the object produce tomographic blurring that is symmetrical about the object. (b) The blurring geometry and image pixel definition are such that the central point of the blurred object falls at the same pixel row and column in all image planes (shown with a thick dark line).

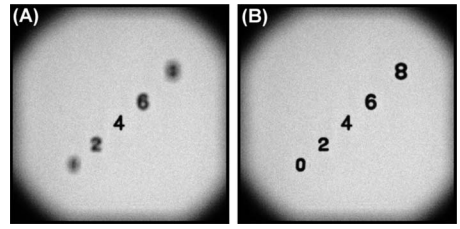

FIG. 3. Phantom demonstration of the SBDX multiplane composite display. The phantom consists of lead numbers spaced at 2 in. intervals along the source-detector axis (number "0" closest to the source). (a) SBDX single plane tomosynthetic reconstruction of a plane 4 mm above the number "4." (b) SBDX multiplane composite image generated from single plane images with 12 mm spacing.

try, with the isocenter located 450 mm above the source plane and 400 mm above the collimator exit surface. The full field-of-view can be continuously scanned and reconstructed at up to 30 frames/s. In this study, imaging was performed at 15 frames/s using 71×71 collimator holes and the isocenter field-of-view was 11.4 cm$\times$11.4 cm. The effective pulse width in this imaging mode is 9.4 ms.[10] The maximum beam current is 220 mAp at 100 kVp and 203 mAp at 120 kVp.[11]

As the focal spot is scanned from hole to hole, detector images are captured and sent to a reconstruction engine. The reconstruction engine contains a set of identical hardware channels which simultaneously perform shift-and-add digital tomosynthesis in real-time at multiple planes parallel to the target surface. The current hardware configuration provides 16 planes. The plane position reconstructed by each channel is programmable. Typically, a stack of 16 planes separated by 12 mm and centered on the gantry isocenter is reconstructed. Implementation details of the tomosynthetic reconstruction may be found in Ref. 10. In the 71×71 hole scanning mode, each image plane has 710×710 pixels. Pixel size is 0.161 mm in the isocenter plane and follows the relationship $p=(\Delta_S/10)[1-(z/Z_D)]$, where z is the source plane to reconstruction plane distance, Δ_S is the focal spot pitch, and Z_D is source to detector distance.

Each reconstructed plane has the property that in-plane objects appear in focus and out-of-plane objects are progressively blurred the farther out of the plane they reside (Fig. 2). A single tomosynthetic plane is inconvenient for interventional cardiac procedures (e.g., angioplasty) since it does not display all anatomy and devices in focus simultaneously. To obtain an image display analogous to that of a conventional fluoroscopic system, with all features presented in focus, the reconstructed planes are combined into a multiplane composite image.

To form the multiplane composite image, first a "score image" is produced for each reconstructed plane. A score image indicates the degree of focus at each (row, column) position in the tomosynthetic image and is calculated from the local image gradient magnitudes (detailed below). Next, the score images are compared. At each (row, column) position, the plane containing the maximum score is located. Last, the composite image is formed from the original tomosynthetic image stack using the pixel value from the plane of highest focus at each pixel position. This technique has been reported in anthropomorphic phantom, animal, and human subjects.[10,11,13] Figure 3 compares an SBDX single plane image to a multiplane composite image of the same object.

II.B. 3D catheter tracking algorithm

The general procedure for 3D localization of objects in a frame period is: (i) Reconstruct tomosynthetic images at regularly spaced planes throughout the volume of interest. (ii) Generate a score image for each tomosynthetic image. (iii) Segment the stack of score images into regions occupied by objects to be tracked. (iv) For each detected object region, analyze score data and calculate a 3D coordinate representing the object center. This is repeated for each scan frame, resulting in a set of (x,y,z) coordinates for each frame period.

II.B.1. Plane scoring

The first two steps of tracking, reconstruction at a set of fixed planes and plane scoring, are designed to reuse image data and methods already used by the SBDX reconstructor to produce a real-time multiplane composite display. The general scoring procedure is outlined in Fig. 4(b). The tomosynthetic image is prefiltered with a rectangular 2D kernel (K_1) of adjustable width. The intent of the prefilter K_1 is to suppress image gradients created by pixel noise while at the same time preserving object gradient information. The K_1 kernel is generally smaller than the object being tracked. Vertical and horizontal gradient images are calculated by filtering with Prewitt gradient kernels and then the absolute gradient values are averaged at each pixel position. Optionally, the score image may be downsampled by averaging over 2×2 blocks of pixels. Although downsampling is not required for catheter tracking, it was performed in this study to mimic the behavior of the current SBDX reconstructor.

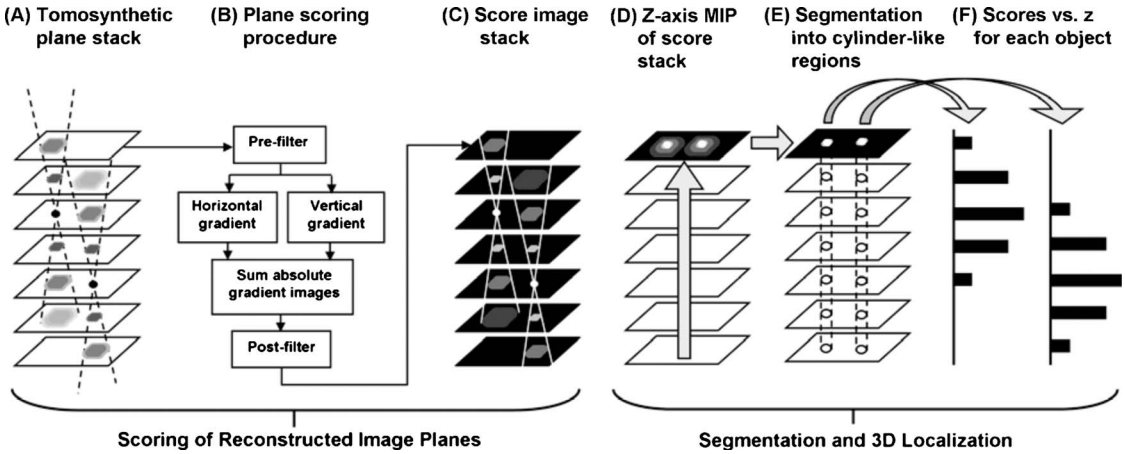

FIG. 4. Overview of the SBDX tracking algorithm. [(a)–(c)] Score images are generated from the tomosynthetic images reconstructed at planes spaced throughout the volume of interest. (d) A MIP of the score data is formed and connected component labeling is applied to the MIP. (e) Each detected object (connected component) defines a cylinderlike region in the imaging volume. The row and column coordinates of an object are calculated from the MIP. (f) The z-coordinate is calculated from the scores versus z-plane inside the object cylindrical region.

Gradient filtering results in an image with scores located mostly along object edges (with higher contrast objects generating higher scores). The subsequent segmentation of the score data into object-centered regions is aided if these scores are spread over the object area. Therefore, in the final step of plane scoring, a second adjustable rectangular 2D filter (K_2) is applied to smooth and spread edge gradients over the object. The size of the K_2 kernel is related to the size of the object.

Figure 5 shows example tomosynthetic images and the corresponding score images for the catheter motion study reported in this paper. The prefiltering and postfiltering kernel sizes are free parameters in the catheter tracking algorithm. The tuning of these filters is described in Sec. III C.

Note that if a catheter tip is guided through a background with varying intensity (e.g., diaphragm, lung, and spine), then even though the tip may have fixed contrast, the image gradient magnitude at the tip will vary in proportion to the local background intensity. This poses a problem during the segmentation step, which uses a fixed score threshold to detect objects. To facilitate the use of a single threshold, independent of background intensity, two intensity lookup tables are added to the above scoring procedure. Before the first filtering step, the tomosynthetic image values are passed

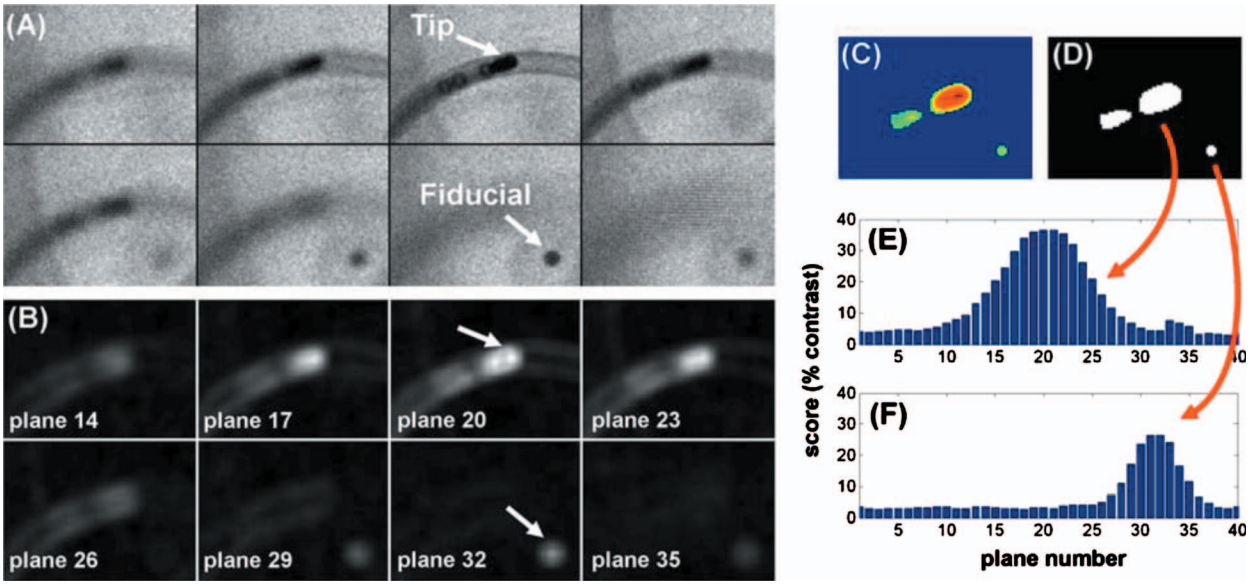

FIG. 5. Demonstration of SBDX tracking for an ablation catheter tip and a fiducial attached to the anterior chest surface (arrows). A total of 40 image planes were reconstructed in this example, with 12 mm spacing. (a) A fixed ROI at eight different reconstructed planes demonstrates progressive out-of-plane blurring (plane numbers 14, 17, 20, 23, 26, 29, 32, and 35 are shown). (b) Score image regions corresponding to the image regions shown in part (a). (c) Maximum intensity projection of the full score stack, with values below the object detection threshold set to zero. (d) Result of connected component labeling. [(e) and (f)] Score versus z-plane distributions for the tip and fiducial, respectively, prior to subtraction of the baseline.

through a log lookup table $y=\ln(x)$. This converts the image intensity to units proportional to the x-ray attenuation line integral and gives the subsequently calculated absolute gradient image units of pixel-to-pixel difference in the attenuation line integral. These pixel-to-pixel differences in attenuation are then converted to units of "edge contrast," ranging from 0% to 100%, by passing the absolute gradient image through a second lookup table $y=100[1-\exp(-x)]$.

II.B.2. Segmentation and localization

For the third and fourth steps of tracking, segmentation and 3D localization, two different approaches have been studied.[12] In the method employed in this paper and shown in Fig. 4, it is assumed that the patient is imaged in a radiographic projection such that catheter electrodes are not overlapping or viewed end-on in the live fluoroscopic display. A maximum intensity projection (MIP) of the score stack is generated along the source-detector direction

$$M(u,v)=\max_z S(u,v,z), \tag{1}$$

where S represents the score stack data, M is the score MIP, and the discrete variables u, v, and z are, respectively, pixel column number, pixel row number, and z-plane coordinate. A matching binary image is generated with values of 1 where the score MIP equals or exceeds a specified object detection threshold T_1.

$$B(u,v)=\begin{cases}1 & \text{if } M(u,v)\geq T_1\\ 0 & \text{otherwise}\end{cases}. \tag{2}$$

The object detection threshold T_1 rejects gradients due to background noise, and also serves to separate neighboring local maxima in the score MIP (e.g., different catheter electrodes) into distinct regions. Distinct groups of pixels in image (u,v)-space are then identified by applying 2D connected component labeling to the binary image $B(u,v)$.[14] Each grouping of pixels defines a 3D cylinderlike segment in (u,v,z)-space, as shown in Fig. 4(e).

To determine the object's 3D coordinate, the scores inside the segmented object region are treated as a probability distribution function. Coordinates in the column and row directions (analogous to x and y coordinates) are determined by calculating the center-of-mass of object pixels in the score MIP. If a detected object occupies a set of N pixels in the score MIP, with (u,v)-coordinates designated as (u_i,v_i), i.e., (u_1,v_1), (u_2,v_2),… (u_N,v_N), then the object coordinates in the column and row directions are given by

$$u_{\text{obj}}=\sum_i M(u_i,v_i)u_i/\sum_i M(u_i,v_i), \tag{3}$$

$$v_{\text{obj}}=\sum_i M(u_i,v_i)v_i/\sum_i M(u_i,v_i). \tag{4}$$

The object z-coordinate is calculated from the distribution of the scores versus z-plane at positions inside the segmented object region [Fig. 4(f)]. To construct this distribution, first the scores in the cylinderlike object region are extracted, a specified baseline value T_2 is subtracted from each pixel score, and negative results are set to zero.

$$S_{\text{obj}}(u_i,v_i,z)=\begin{cases}S(u_i,v_i,z)-T_2 & \text{if } S(u_i,v_i,z)\geq T_2\\ 0 & \text{otherwise}\end{cases}. \tag{5}$$

The baseline T_2 determines how many planes contribute to the z-coordinate and also rejects background gradients. Then the results are averaged at each plane to produce the score versus z-plane distribution for the object.

$$f_{\text{obj}}(z)=\frac{1}{N}\sum_i S_{\text{obj}}(u_i,v_i,z). \tag{6}$$

The object z-coordinate is the center-of-mass of this distribution

$$z_{\text{obj}}=\sum_z f_{\text{obj}}(z)z/\sum_z f_{\text{obj}}(z), \tag{7}$$

where the summation is over the discrete plane positions z, measured from the target surface in the x-ray source to the plane of reconstruction.

Figure 5 shows an example thresholded score MIP, the result of connected component labeling, and two score versus z-plane distributions prior to subtraction of the baseline T_2. The value of the object detection threshold T_1 is tuned to the objects being tracked (see Sec. III C). The baseline value T_2 is also adjustable. In this study, we set T_2 to approximately 2/3 of the peak in the score versus z-plane distribution for an object. Baseline subtraction ensures that a reasonably low number of planes contribute to the calculation of the z-coordinate (typically 7–8 around the object) and that the postsubtraction distribution is symmetrical in shape (i.e., not influenced by the constant background level or asymmetries that may exist in the tails of the distribution).

The algorithm exploits two properties of the SBDX tomosynthetic blurring geometry and image reconstruction (Fig. 2). First, tomosynthetic blurring is symmetric about the object's true position. z-positions can be determined with higher precision than the plane spacing by calculating a weighted average of object focus versus z-plane. Second, the image of an object remains centered on a fixed column and row, regardless of plane position. This allows segmentation to be performed in (u,v)-space.

After all the segmented object regions have been processed in the manner described by Eqs. (3)–(7), the set of (u,v,z) coordinates corresponding to detected objects is mapped to an (x,y,z) coordinate system. This is accomplished using 3D linear interpolation and the known (x,y,z) coordinates of all the pixels in the score image stack. The (x,y,z) coordinate system is right handed, defined with the origin at the center of the target surface, z increasing toward the detector, x increasing to the right in the image display (patient left in supine position) and y increasing to the top of the image display (patient superior).

III. METHODS

To evaluate the accuracy and precision of SBDX catheter tracking, two phantom studies were conducted on the SBDX

TABLE I. Cardiac electrophysiology catheters used in this study.

Label	Catheter type	No. of electrodes	Tip electrode		Proximal electrodes		Max, min gap between electrodes (mm)
			Length, diameter (mm)	Image contrast (%)	Length, diameter (mm)	Image contrast (%)	
A	Ablation (7 Fr)	4	3.9, 2.3	96	1.1, 2.3	86	5.3, 2.0
B	Ablation (8 Fr)	4	3.5, 2.4	96	1.5, 2.7	85	3.0, 0.9
C	Ablation (8 Fr)	4	8.0, 2.7	97	1.3, 2.3	84	2.7, 2.4
D	Diagnostic (5 Fr)	4	2.1, 1.7	95	2.3, 1.7	91	4.5, 1.9
E	Coronary sinus (6 Fr)	10	2.0, 2.0	95	2.1, 2.0	92	4.5, 2.1
F	Circular mapping (7 Fr)	10	2.8, 0.9	61	0.9, 1.5	52	

prototype at the University of Wisconsin-Madison. In the first study, an ablation catheter inside a chest phantom was tracked at different speeds as it was pulled along a fixed 3D trajectory. Tracking results were registered to and compared to a volume CT of the chest phantom. In the second study, tracking was performed at different image intensities and signal-to-noise ratios for six stationary catheters. Table I lists the different catheter types and geometries used. Figure 6 shows an SBDX x-ray image of the catheters. The specifications of the SBDX system have been previously reported.[10,11]

III.A. Moving catheter tip in chest phantom

A phantom was constructed to mimic the anatomy and catheter trajectory typical of catheter ablation for the treatment of left atrial fibrillation. A hollow cardiac chamber phantom (Venous Sam, LFA Anatomicals, Lake Forest, IL) was placed inside a chest phantom consisting of plastic with embedded ribs and spine (Fig. 7). A trans-septal catheter sheath (Agilis 12 Fr, St. Jude Medical, St. Paul, MN) was attached to points inside the cardiac phantom to define a reproducible catheter trajectory from the femoral vein, up the inferior vena cava, into the right atrium, across the septum, and into the left atrium. Catheter "A" was advanced up the sheath so that the tip was located in the left atrium and the proximal end was attached to a linear motion stage to perform constant-speed catheter pullbacks.

SBDX tracking results for the catheter tip were compared to the 3D volume of the confining catheter sheath determined from a CT scan of the phantom. To facilitate the registration of the SBDX and CT coordinate systems, fiducials were attached to points on the anterior and posterior chest walls. Each fiducial consisted of a nylon nut, attached to the phantom, and a matching nylon screw with a 2.4 mm diameter steel ball bearing at the center of the screw head.

The SBDX gantry was placed in posterior-anterior orientation and the phantom was centered at the gantry isocenter. Three imaging runs were performed with the catheter pullback speed programed to 10, 25, and 50 mm/s. For reference, the majority of velocities observed at landmarks on the coronary arteries fall within the range 10–50 mm/s.[15] Scanning was performed in 71×71 hole, 15 frames/s mode, which provided an 11.4 cm wide image at gantry isocenter. The x-ray source was operated at 100 kVp. Beam current was adjusted such that the detected fluence at the isocenter plane ranged from 1121 to 2244 photons/mm^2 in the vicinity of the catheter, depending on location within the field-of-view (29.1–58.2 photons/pixel). Image intensity was similar to that previously measured with 26–30 cm acrylic attenuation at maximum beam current (220 mAp at 100 kVp).[11] The chest phantom itself provided 10–14 cm of acrylic attenuation depending on catheter location. An additional 2.3 cm acrylic plus 0.5 mm Cu was placed in front of the x-ray

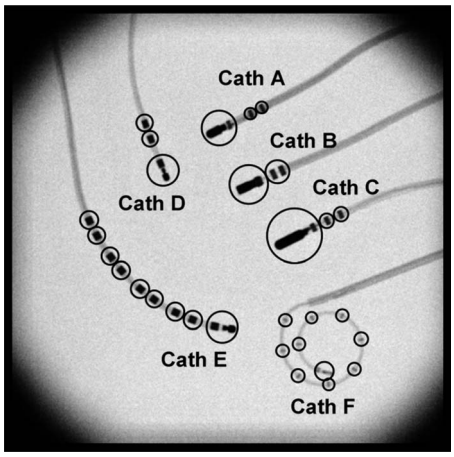

FIG. 6. SBDX image of catheters A–F. Circles indicate regions that were independently tracked in 3D space.

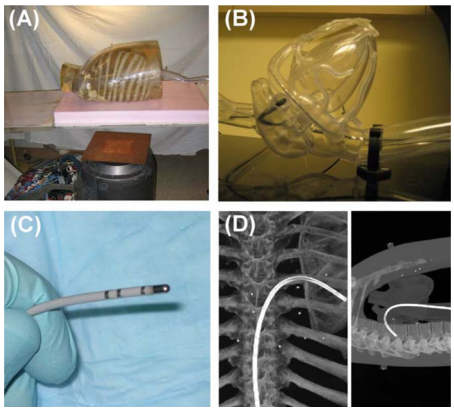

FIG. 7. (a) Chest phantom placed on an x-ray table and supporting foam. The SBDX x-ray source is below. (b) Cardiac phantom and catheter sheath prior to placement inside the chest phantom. (c) Tip of ablation catheter A. (d) CT images of the chest phantom showing catheter sheath.

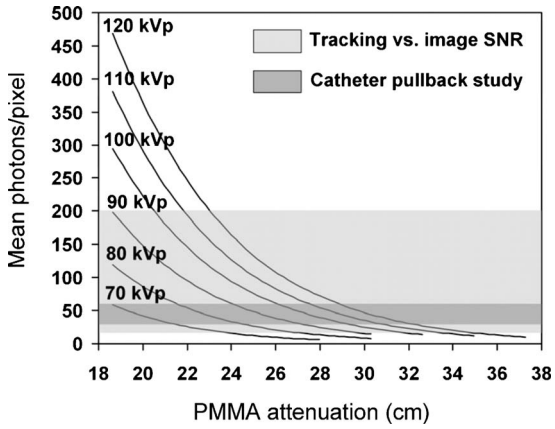

FIG. 8. Mean image fluence during catheter tracking studies (shaded regions) compared to the mean image fluence measured versus acrylic phantom thickness and kVp on the SBDX prototype system (lines; Ref. 11).

source for beam hardening. The total filtration was estimated to produce an x-ray spectrum shape similar to that exiting at least 30 cm acrylic.[16] The beam current was 21.3 mAp.

Raw SBDX detector images generated during each imaging run were recorded to a memory board in the SBDX prototype hardware reconstructor. After the experiment, the data were transferred to an external workstation for offline image reconstruction and catheter tracking. This method was used because the catheter tracking algorithm was not part of the hardware reconstructor. Image reconstruction, catheter tracking, and selection of adjustable tracking parameters are described in Sec. III C.

The CT scan of the phantom was performed on a 64 detector row scanner (Lightspeed VCT, GE Healthcare, Waukesha, WI) with the catheter removed and the sheath left intact (120 kVp, 295 mA, 0.984:1 helical pitch, 0.5 s rotation). To minimize streaking in the CT images, the fiducial screw heads were swapped out for identical ones containing 2.4 mm aluminum ball bearings. Axial images were reconstructed with 0.625 mm slice thickness and 0.488 mm in-plane voxel width. The CT images were exported in DICOM format for analysis. The comparison of the SBDX-tracked catheter tip trajectory to the CT-derived sheath volume is described in Sec. III D.

III.B. Catheter tracking versus image SNR

Previous simulation studies[12] found that object tracking precision along the z-axis (source-detector direction) depends on image noise magnitude, with the z-coordinate standard deviation increasing as the mean detected fluence decreases. A wide range of fluences are encountered clinically, depending on patient size, anatomic region, radiographic projection, and x-ray source technique. Figure 8 shows the mean detected fluence in photons/pixel as a function of kVp and acrylic phantom thickness for the SBDX prototype in 71×71 hole, 15 frames/s scanning mode (max power).[11] Furthermore, tracking precision can depend on the contrast and size of the electrodes/markers in a catheter.

To investigate the relationship between tracking precision, image noise level, and catheter element contrast and size, SBDX imaging runs were acquired at different image intensities with six different catheters affixed to the x-ray table. Three of the catheters were four-electrode EP ablation catheters ("A," "B," and "C"). The other three catheters were a four-electrode EP diagnostic catheter ("D"), a ten-electrode coronary sinus mapping catheter ("E"), and a ten-element circular mapping catheter ("F"). The gantry was in posterior-anterior orientation and the table surface was approximately at gantry isocenter. The experimental setup placed the catheters in a common plane approximately parallel to the target in the x-ray source.

The x-ray source was operated with the same scan mode, kVp, and mAp that was used in the moving catheter chest phantom study (Sec. III A). Six imaging runs of 30 frames each were acquired, using uniformly attenuating acrylic phantoms of 7.0, 9.3, 11.7, 14.0, 16.3, and 18.6 cm acrylic (plus 0.5 mm Cu filtration in all cases). The acrylic was distributed above and below the plane of the catheters. Depending on phantom thickness, the mean detected image fluence ranged from 7625 to 662 photons/mm^2 at isocenter (198–17.2 photons/pixel). Figure 8 shows the mean image fluences in this image SNR study and also the range of fluences measured from the moving catheter chest phantom study (darker spine region versus bright atrial region).

III.C. Image reconstruction and catheter tracking

In this first study, SBDX catheter tracking was performed in software written in MATLAB (MathWorks, Natick, MA) at the University of Wisconsin-Madison. The software accepted the raw detector data acquired during SBDX imaging, reconstructed a stack of tomosynthetic images for each frame period (emulating the SBDX reconstruction hardware), and then performed the plane scoring, segmentation, and localization steps described in Sec. II B. The tomosynthetic plane stack, score stack, and 3D coordinates of detected objects were saved for each frame period.

Tomosynthetic images were reconstructed at fixed plane positions spaced by 12 mm and centered on the phantom. As discussed in Sec. II, the hardware reconstructor of the SBDX prototype can reconstruct 16 planes simultaneously in real-time. During tracking, typically seven to eight planes about an object will contribute to the object's 3D coordinate calculation. In the study of stationary catheter tracking precision versus SNR (Sec. III B), 16 plane positions were reconstructed. In the study of a moving catheter in a chest phantom (Sec. III A), extra planes were added to enable simultaneous tracking of the fiducials placed on the anterior and posterior chest surfaces. Therefore, the moving catheter experiment used a stack of 40 planes centered on the chest phantom. All plane stacks were positioned so that one plane coincided with the isocenter plane.

The catheter tracking algorithm has two adjustable filters in the plane scoring stage (K_1 and K_2) and two adjustable thresholds in the segmentation and localization stage (T_1 and T_2). Although these parameters could be tuned to individual

catheter element shapes and orientations, an effort was made to identify a single combination of parameters that would enable tracking for all elements on a catheter. An effort was also made to use common tracking parameters across different image scenes and different catheter types where feasible.

Initial investigations were conducted using a range of square filter kernel sizes (1–22 pixels wide) and a range of threshold values (5%–55%) with sample image frames. The performance of each filter combination (K_1 and K_2) was evaluated by examining two effects: (i) The peak score value at the object relative to the scores in a background region and (ii) the number of valid object detection thresholds that the filtering enabled, where a threshold is considered valid if it results in detection of the correct number of catheter elements. For prefiltering, it was decided to use $K_1 = 5 \times 5$ (0.8 mm wide at isocenter), which showed good performance for a number of catheters. The postfiltering kernel K_2 was adjusted depending on which catheters were in the imaging field. It was found that segmentation was aided if the postfiltering kernel size was similar to the object size and not significantly larger than the smallest dimension of the object as it appeared in the image. The selected value for T_1 was the midpoint of the valid range of thresholds for the selected filter combination. The T_2 value was set to approximately 2/3 of the peak in the score versus z-plane distribution.

Note the postfiltering step was performed on score images that were downsampled via 2×2 block averaging. For the sake of consistency, all filter kernel sizes are reported in units of input tomosynthetic image pixels. The width of the kernel in mm at the isocenter plane is also reported for reference.

III.D. Evaluation of tracking performance

III.D.1. Moving catheter tip tracking

The set of 3D points generated by SBDX catheter tip tracking during a pullback was compared to the known 3D volume of the confining catheter sheath determined from the CT scan. Details of the SBDX-to-CT registration, sheath segmentation, and sheath centerline calculation are provided below. For each image frame, the 3D tip-to-centerline distance was calculated, defined as the distance between a tracked catheter tip position and the nearest point on the sheath centerline. Results are reported as the average value over all frames $\pm$one standard deviation. Tracking results were analyzed when the tip was moving and within the central 92% of the image field-of-view. The fraction of all SBDX-tracked points falling within the sheath volume was also calculated and for points falling outside of the sheath, the tip-to-sheath surface distance was calculated. Last, the average speed of the catheter along its tracked 3D trajectory was calculated and compared to the programmed speed. The average speed was calculated after performing five-frame moving average on the catheter trajectory (0.33 s temporal window) to minimize the influence of coordinate fluctuations.

A rigid 3D rotation/translation transformation matrix between the SBDX and CT systems was calculated from seven fiducial positions.[17] The 3D position of a fiducial in SBDX coordinates was determined by averaging tracking results within a cylindrical volume of interest around the fiducial. The corresponding 3D position in CT coordinates was determined by locating the fiducial within the CT image volume and calculating its intensity-weighted center-of-mass, ignoring values below 300 HU.

The CT voxels contained within the sheath wall and lumen were identified using a combination of edge detection and intensity-based segmentation. The 3D centerline of the sheath was determined by skeletonizing the segmented volume (sheath plus lumen) using a homotopy-preserving flux-driven algorithm.[18] A 3D smoothing spline curve was fit to the skeleton voxel positions to obtain a sheath centerline representation with subvoxel precision. The smoothing spline was evaluated at points spaced evenly by 0.075 mm along the 3D curve.

III.D.2. Catheter tracking versus image SNR

Cylindrical ROIs were defined around elements in a catheter and the 3D tracking coordinates versus frame were extracted for each element. Mean and standard deviation in the tracked position were calculated in the x, y, and z directions. As seen in Fig. 6, the tip electrode and first proximal electrode on a catheter are often bridged by an internal high-contrast component or are very close together. Therefore, the tip and first proximal electrode were tracked as a single object (this was also done for the chest phantom study). z-coordinate results are reported for each tip ROI. For the remaining proximal elements in a catheter, the z-coordinate mean and z-coordinate standard deviation measured from the individual ROIs were averaged across ROIs. Averaging was performed since proximal elements in a catheter were of identical shape. Standard deviation in the x and y directions were similar and results are reported as the maximum standard deviation in either direction.

IV. RESULTS

IV.A. Moving catheter tip in chest phantom

SBDX catheter tip tracking during a 10 mm/s pullback is compared to the CT-derived catheter sheath volume in Fig. 9. The figure shows a single SBDX tomosynthetic image frame during pullback and the 3D tip tracking results for all frames from three different perspectives. All tip tracking results have been registered to the CT coordinate system using a transformation derived from the tracked fiducial positions. Note the example tomosynthetic image planes and score images shown in Fig. 5 are a region of interest from the same image frame shown in Fig. 9(a). The 3D tip trajectory produced by the SBDX tracking algorithm closely followed that of the catheter sheath volume determined from CT.

Figure 10 shows the components of the tip trajectory along the x-axis (phantom right-to-left), y-axis (inferior-to-superior), and z-axis (posterior-to-anterior, also the source-detector axis of SBDX) for 10, 25, and 50 mm/sec catheter pullback speeds. The 3D distance between the tracked tip position and the sheath centerline is shown next to each trajectory figure. For the 10 mm/s pullback, the tip-to-centerline

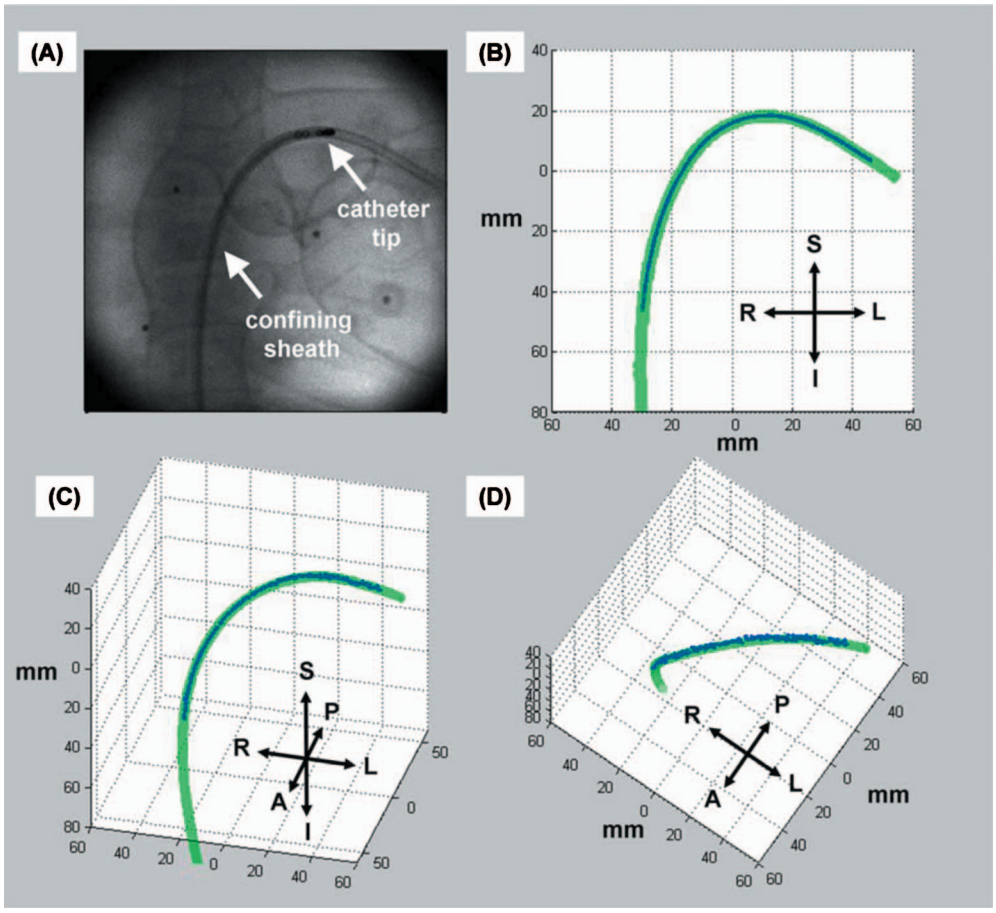

FIG. 9. (a) Example tomosynthetic image during a 10 mm/s catheter pullback. [(b)–(d)] Tip tracking coordinates for all image frames (blue points) compared to the catheter sheath volume (green). The comparison is shown from three perspectives. The right-left (R-L), inferior-superior (I-S), and posterior-anteior (P-A) axes are shown for reference.

distance was 0.9 ± 0.7 mm and 83% of all tracked tip positions were located inside the catheter sheath volume. The 25 mm/s pullback yielded 1.1 ± 0.9 mm tip-to-centerline distance and 78% of tip positions inside the sheath volume. The corresponding 50 mm/s pullback results were 0.9 ± 0.6 mm and 88%. The tip position was localized in every image frame analyzed (332 frames total for three imaging runs). The tip trajectory spanned 55 mm along the z-axis, 76 mm along the x-axis, and 65 mm along the y-axis. The trajectory was intersected by five of the reconstructed planes. Results clearly demonstrate that 3D tracking coordinates can be obtained with precision finer than the plane-to-plane spacing (12 mm).

Averaged over 10–50 mm/s pullback speeds, the tip-to-centerline distance was 1.0 ± 0.8 mm and 83% of tracked positions were inside the sheath. Tip positions outside the sheath were within 0.6 ± 0.5 mm of the sheath surface. Tip-to-centerline distances were comparable to the diameter of the ablation catheter tip (2.3 mm). Note that tip-to-centerline results include errors introduced by the SBDX-to-CT coordinate transformation. In this study, a simple rigid transformation was derived from seven fiducial positions on the chest wall. Registration error was estimated to be ± 0.7 mm, calculated as one standard deviation in the individual distances between the transformed SBDX fiducial position and the CT fiducial position. Frame-to-frame tracking precision also depends on the image SNR in the vicinity of the catheter tip. Image intensity ranged from 58.2 photons/pixel at the start of the trajectory (atrium region) to 29.1 photons/pixel at the end of the trajectory (spine region). This variation in image intensity along the trajectory is consistent with the observation that tip-to-centerline distance tended to increase and show more frame-to-frame deviations near the end of the catheter pullbacks (see Fig. 10).

The average speeds calculated from the tip trajectories were 10.5, 24.8, and 47.6 mm/s. The SBDX-tracked tip speeds were all within 5% of with the programmed catheter pullback speeds. The tip tracking parameters for all catheter pullbacks were: Prefilter $K_1 = 5 \times 5$ (0.8 mm), postfilter $K_2 = 22 \times 22$ (3.5 mm), detection threshold $T_1 = 25\%$, and z-distribution baseline $T_2 = 25\%$. The fiducial tracking parameters were: $K_1 = 5 \times 5$ (0.8 mm), $K_2 = 14 \times 14$ (2.3 mm), $T_1 = 20\%$, and $T_2 = 15\%$.

IV.B. Tracking precision versus image noise and catheter geometry

The z-coordinate for each of the six stationary catheter tips is shown in Fig. 11 as a function of the mean background

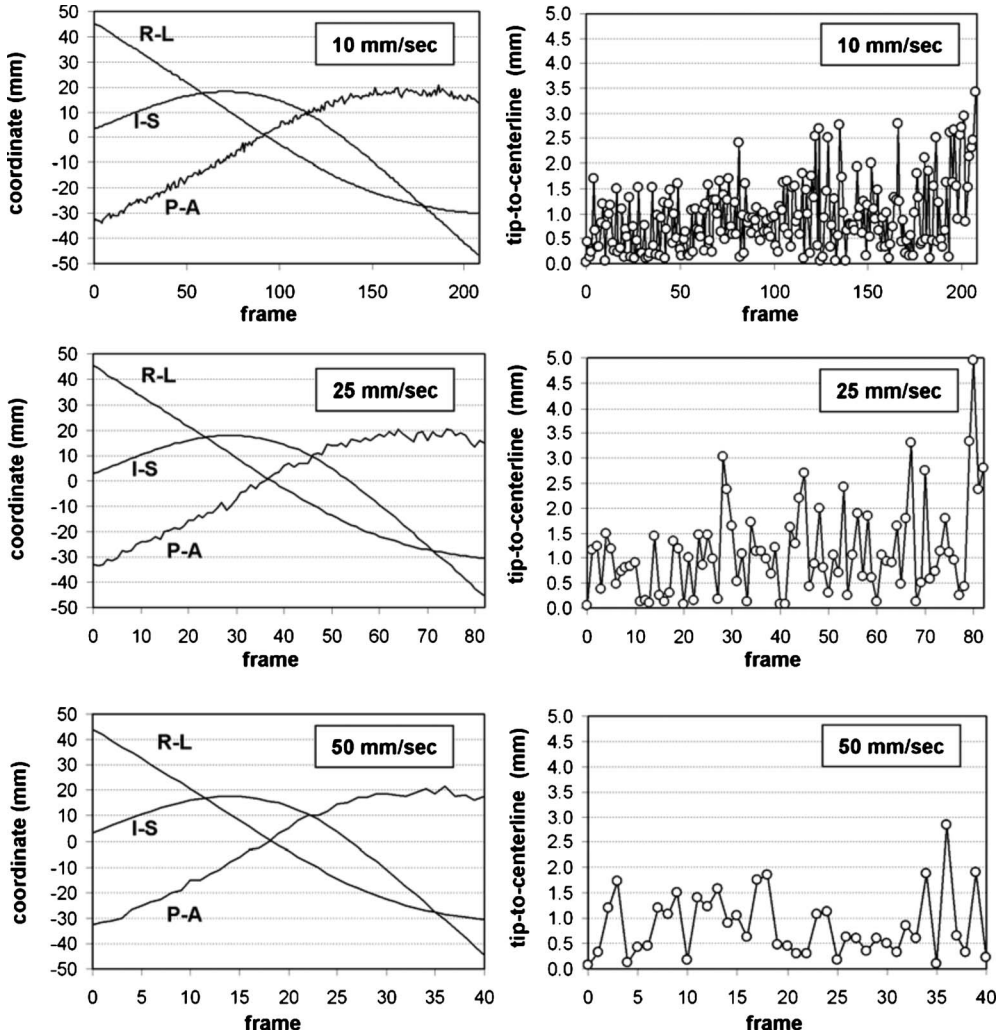

FIG. 10. Tip tracking results for 10 (top row), 25 (middle row), and 50 mm/s (bottom row) catheter pullbacks along a fixed 3D trajectory in a chest phantom. The left column shows the tracked tip position versus image frame in the right-left (R-L), inferior-superior (I-S), and posterior-anterior (P-A) directions. The right column shows the 3D distance from catheter tip-to-sheath centerline, versus image frame.

image intensity. The symbols represent the mean position over 30 frames; the error bars represent ±one standard deviation. The catheters were coplanar but not all at the same z-coordinate. All analysis ROIs are indicated on Fig. 6. Table I lists the measured length, diameter, and in-plane image contrast for the catheter electrodes. The tip electrodes of the ablation, diagnostic, and coronary sinus catheters (A–E) had 95%–97% contrast, lengths from 2.0 to 8.0 mm, and diameters from 1.7 to 2.7 mm. Catheter F, a circular mapping catheter, had smaller, lower contrast (52% to 61%) electrodes.

The same set of adjustable tracking parameters was used for all elements within a catheter. Furthermore, a single set of parameters was used for catheters A–E, which enabled simultaneous tracking of these catheters. Figure 11 shows an example of simultaneous 3D tracking of the five catheters. The tracking parameters were: $K_1=5\times5$ (0.8 mm), $K_2=10\times10$ (1.6 mm), $T_1=30\%$, and $T_2=20\%$. Since catheter F contained lower contrast electrodes, the threshold values for this catheter were set to $T_1=12\%$ and $T_2=8\%$ and tracking was performed separately.

Figure 12 shows the standard deviation in catheter tip z-coordinate versus image fluence. As expected, the z-coordinate precision improved as the detected image fluence increased. With catheter A (also used in the moving catheter chest phantom study), the z-coordinate standard deviation ranged from 0.8 to 0.2 mm for background intensities from 17.2 to 198 photons/pixel. The tracking precision was similar to that observed in the chest phantom study. The trend in tip tracking z-precision versus image intensity was similar for catheters A–E. For these catheter tips and all imaging conditions, the highest and lowest z-coordinate standard deviations were 0.9 and 0.2 mm. The tracking of catheter tip F was less precise, with the z-coordinate standard deviation ranging from 1.6 mm to 0.4 mm.

The z-coordinate standard deviations for the proximal electrodes are shown in Fig. 13. As with the tips, there was a trend of improving precision as image intensity increased and there was a difference between catheters A–E and catheter F. In any given catheter, the proximal electrodes were tracked with somewhat lower z-coordinate precision than the tip. The ratio of proximal deviations to tip deviations ranged

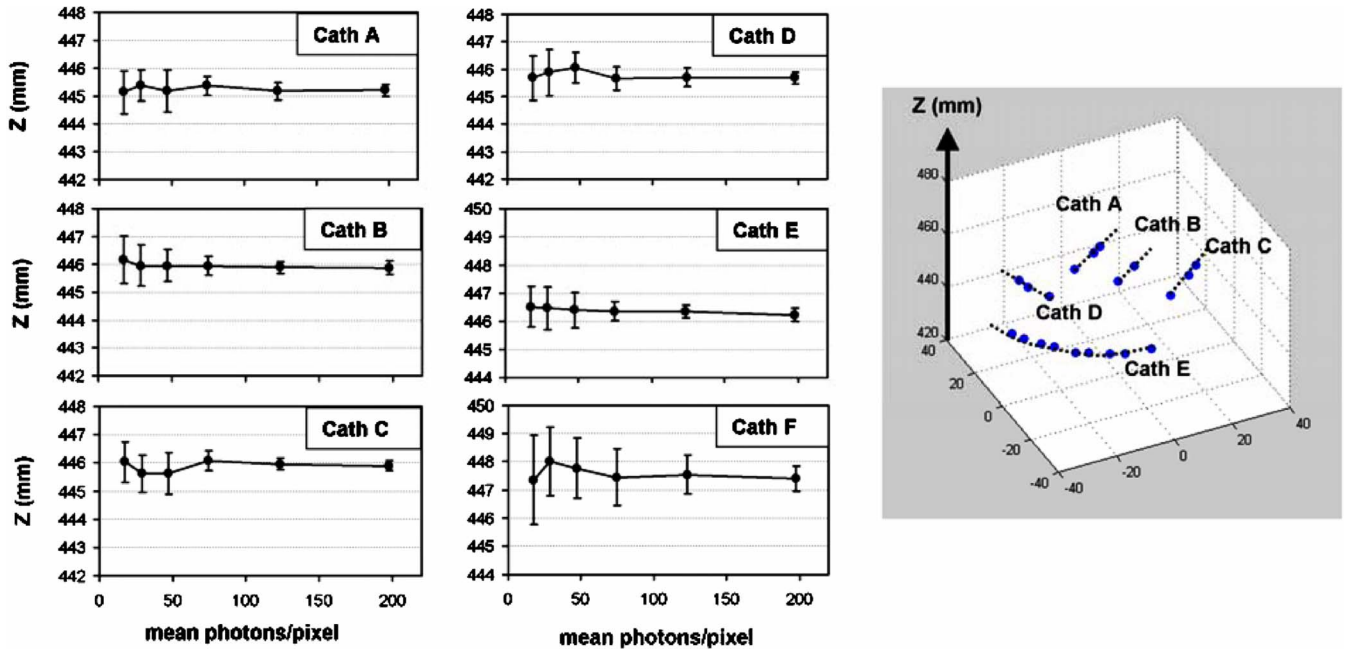

FIG. 11. Tip tracking in the z-direction (source-detector axis) versus mean image fluence for six different catheters. Symbols indicate the mean z-coordinate over 30 image frames; error bars indicate $\pm$one standard deviation in the individual z-coordinates. The figure on the far right demonstrates simultaneous tracking of elements in catheters A–E.

from 1.33 (catheter B) to 2.25 (catheter C). The difference is believed to be due to the fact that proximal electrodes are smaller than the tip and yield fewer gradient estimates over the electrode perimeter. The proximal electrodes also had slightly lower image contrast (e.g., 84%–92% for catheters A–E).

The maximum standard deviation in the x and y directions was 0.1 mm for any element of catheters A–E in any imaging scenario. For catheter F, the maximum standard deviation in x or y was 0.4 mm. Therefore the greatest uncertainty in 3D coordinate is in the z-direction (source-detector axis). This can be understood as the result of the relatively narrow tomographic angle of the SBDX system.

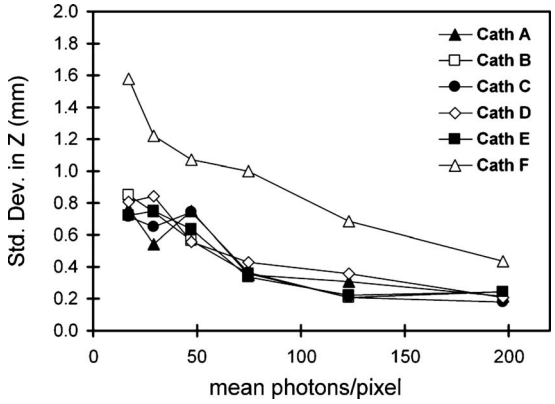

FIG. 12. Standard deviation in catheter tip z-coordinate versus mean image fluence.

V. DISCUSSION

Fluoroscopic x-ray imaging is the foundation of many interventional procedures but it carries with it the potential to deliver high x-ray dose. SBDX is designed to provide fluoroscopic imaging at a substantially reduced dose rate compared to conventional fluoroscopic systems.[11] Dose reduction is achieved, in part, by the inverse geometry configuration of a large-area scanned source and small-area detector. The resulting reconstructed image is planar tomographic in nature and this fact can be exploited to provide the depth information valuable in many interventional procedures, such as the cardiac RF ablation procedures that are the focus of this study. A previous simulation work predicted that the SBDX catheter tracking algorithm described in this paper would enable 3D catheter tracking with accuracy and precision of approximately 1 mm or better.[12] The phantom studies reported here, which were conducted on an SBDX prototype system with a variety of catheter geometries, trajectories, velocities, background features, and image intensities, confirm this prediction.

SBDX catheter tracking is compatible with standard catheters containing high-contrast markers, can follow multiple markers and catheters in the field-of-view, has temporal sampling equal to the imaging rate (15–30 Hz), uses a single gantry view angle, and does not require geometric calibrations. Since the location of each pixel in each tomosynthetic image plane is precisely known relative to the source and detector, the 3D coordinates are automatically registered to the SBDX gantry. These coordinates can be transformed to a patient-based coordinate system using gantry and table orientation information.

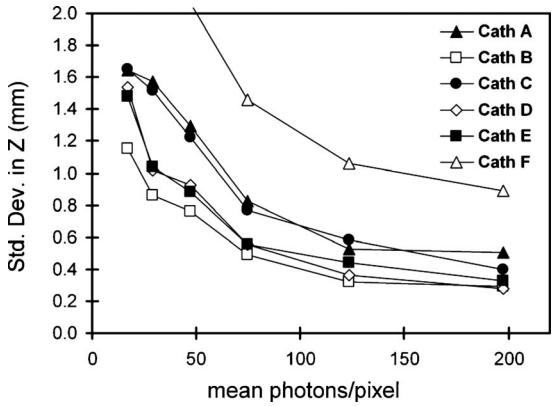

FIG. 13. Standard deviation in proximal electrode z-coordinate versus mean image fluence.

The tracking algorithm is based on the concept that object blurring versus plane position can be treated as a distribution function whose center-of-mass represents the true object position. It is designed to make use of the tomosynthetic reconstructions and plane scoring techniques that were developed for real-time fluoroscopic image display. Tomosynthesis-based 3D localization has been reported in other applications, for example, brachytherapy seed localization.[19] Tracking in cardiac applications is challenging, however, due to the high object velocities involved. To our knowledge, SBDX is the only tomosynthesis system with the scanning speed, x-ray output, and continuous imaging capability required for both live x-ray fluoroscopy and frame-by-frame 3D cardiac catheter tracking.

The SBDX study of a moving ablation catheter in a chest phantom demonstrated 3D tip tracking with 1.0 mm mean error after registering and comparing tracked positions to CT. Imaging was conducted at an intensity similar to that which may be encountered clinically. The study of stationary catheters versus image intensity demonstrated z-coordinate standard deviations ranging from 0.2 to 0.9 mm for ablation and diagnostic catheter tips depending on background image intensity. Smaller deviations were observed in the x- and y-coordinates. Our experiments show that SBDX may offer similar catheter tip tracking accuracy to commercially available nonfluoroscopic EM tracking systems which are in use for radiofrequency catheter ablation procedures. EM tracking systems have been shown to provide <1 mm relative distance error and location standard deviation.[20]

Tracking precision depended on image intensity, catheter electrode size, and electrode contrast. The improvement in tracking precision with background intensity was consistent with expectations. This may be understood as the result of improved object signal-to-noise ratio in each tomosynthetic image, which yields more reliable gradient estimates at any object point, and also a reduction in background gradient values, which gives more freedom in the selection of detection threshold. A previous work has shown that z-axis precision is also dependent on the tomographic angle of the SBDX system.[12] In a detector redesign currently underway, the detector width has been doubled. The increase in both tomographic angle and image SNR anticipated for this new detector is expected to improve tracking precision compared to the SBDX prototype used in this study.

Tracking performance depends on the proper selection of filtering kernels and score thresholds. In this study, several guidelines for the selection of these parameters are presented. Although the algorithm could be optimized to yield the best precision for individual electrodes and electrode orientations, there is value in finding a set of parameters that work for a variety of objects simultaneously. In this study, it was possible to simultaneously track the electrodes on five different catheters across a range of image intensities. Multiple catheter tracking may be useful in a scenario where a navigated catheter tip is tracked relative to a second catheter positioned at an anatomic landmark (e.g., in the coronary sinus).

Several limitations of the tracking algorithm should be noted. The tracking algorithm used here assumes that electrodes are nonoverlapping in the image field-of-view. An alternative algorithm that enables tracking of overlapping objects separated by several cm has been described; however, it is more computationally expensive.[12] We note that the nonoverlapping condition is often satisfied during clinical fluoroscopy since the interventionist generally avoids end-on views. Although a variety of velocities and 3D trajectories were tested in phantoms, true 3D catheter motion in the clinical setting may be more complicated and will include respiratory motion. Studies of tracking performance in animal models are underway.

Ultimately, a real-time implementation of the tracking algorithm is desired. Presently, only multiplane tomosynthesis and plane scoring may be performed in real-time SBDX hardware. Tracking was performed offline in software using detector data recorded and downloaded from the reconstructor. We note that the design of a next generation SBDX system is underway and the real-time reconstruction hardware for that system has been designed to enable both imaging and independent analysis of tomosynthetic plane stacks (e.g., catheter tracking).[21] For a clinical implementation of SBDX catheter tracking, a method for registering tracked 3D coordinates to preacquired volume images (e.g., CT or MR) is also desired. The external fiducial technique used in this study to register SBDX-to-CT is one possibility, as is the use of internal landmarks or internally placed catheters. This is left as a topic for further investigation.

VI. CONCLUSIONS

High speed multiplanar tomosynthesis with an inverse geometry x-ray fluoroscopy system enables accurate and precise 3D tracking of high-contrast electrodes in standard cardiac catheters. Phantom studies with the SBDX prototype system demonstrate catheter tip tracking accuracy and precision of 1 mm or better is feasible. The combination of low dose fluoroscopic imaging and 3D catheter tracking offered by SBDX technology is well-suited to anatomically targeted interventional procedures such as radiofrequency catheter ablation of cardiac arrhythmias.

ACKNOWLEDGMENTS

Financial support for this work was provided by NIH Grant No. R01 HL084022. The authors wish to thank Dr. Douglass Kopp and Dr. Andrew Klein for their helpful discussions and assistance. The authors also thank Triple Ring Technologies, Inc. and NovaRay Medical, Inc. for technical support for the SBDX prototype system.

[a]Author to whom correspondence should be addressed. Electronic mail: speidel@wisc.edu

[1]M. Haïssaguerre, P. Jaïs, D. C. Shah, A. Takahashi, M. Hocini, G. Quiniou, S. Garrigue, A. Le Mouroux, P. Le Métayer, and J. Clémenty, "Spontaneous initiation of atrial fibrillation by ectopic beats originating in the pulmonary veins," N. Engl. J. Med. **339**, 659–666 (1998).

[2]C. Pappone, S. Rosanio, G. Oreto, M. Tocchi, F. Gugliotta, G. Vicedomini, A. Salvati, C. Dicandia, P. Mazzone, V. Santinelli, S. Gulletta, and S. Chierchia, "Circumferential radiofrequency ablation of pulmonary vein ostia—A new anatomic approach for curing atrial fibrillation," Circulation **102**, 2619–2628 (2000).

[3]M. Ouyang, D. Bansch, S. Ernst, A. Schaumann, H. Hachiya, M. Chen, J. Chun, P. Falk, A. Khanedani, M. Antz, and K.-H. Kuck, "Complete isolation of left atrium surrounding the pulmonary veins: New insights from the double-lasso technique in paroxysmal atrial fibrillation," Circulation **110**, 2090–2096 (2004).

[4]T. R. Koenig, D. Wolff, F. A. Mettler, and L. K. Wagner, "Skin injuries from fluoroscopically guided procedures: Part 1, characteristics of radiation injury," AJR, Am. J. Roentgenol. **177**, 3–11 (2001).

[5]K. Chida, H. Saito, H. Otani, M. Kohzuki, S. Takahashi, S. Yamada, K. Shirato, and M. Zuguchi, "Relationship between fluoroscopic time, dose-area product, body weight, and maximum radiation skin dose in cardiac interventional procedures," AJR, Am. J. Roentgenol. **186**, 774–778 (2006).

[6]J. Ector, O. Dragusin, B. Adriaenssens, W. Huybrechts, R. Willems, H. Ector, and H. Heidbuchel, "Obesity is a major determinant of radiation dose in patients undergoing pulmonary vein isolation for atrial fibrillation," J. Am. Coll. Cardiol. **50**, 234–242 (2007).

[7]S. A. Ben-Haim, D. Osadchy, I. Schuster, L. Gepstein, G. Hayam, and M. E. Josephson, "Nonfluoroscopic in vivo navigation and mapping technology," Nat. Med. **2**, 1393–1395 (1996).

[8]J. Dong, H. Calkins, S. B. Solomon, S. Lai, D. Dalal, A. Lardo, E. Brem, A. Preiss, R. D. Berger, H. Halperin, and T. Dickfield, "Integrated electroanatomic mapping with three-dimensional computed tomographic images for real-time guided ablations," Circulation **113**, 186–194 (2006).

[9]E. G. Solomon, B. P. Wilfley, M. S. Van Lysel, A. W. Joseph, and J. A. Heanue, "Scanning-beam digital x-ray (SBDX) for cardiac angiography," Proc. SPIE **3659**, 246–257 (1999).

[10]M. A. Speidel, B. P. Wilfley, J. M. Star-Lack, J. A. Heanue, and M. S. VanLysel, "Scanning-beam digital x-ray (SBDX) technology for interventional and diagnostic cardiac angiography," Med. Phys. **33**, 2714–2727 (2006).

[11]M. A. Speidel, B. P. Wilfley, J. M. Star-Lack, J. A. Heanue, T. D. Betts, and M. S. Van Lysel, "Comparison of entrance exposure and signal-to-noise ratio between an SBDX prototype and a wide-beam cardiac angiographic system," Med. Phys. **33**, 2728–2743 (2006).

[12]M. A. Speidel, A. P. Lowell, J. A. Heanue, and M. S. Van Lysel, "Frame-by-frame 3D catheter tracking methods for an inverse geometry cardiac interventional system," Proc. SPIE **6913**, 691311 (2008).

[13]M. R. Wolff, J. G. Keevil, M. A. Speidel, M. Wilfley, B. P. Wilfley, J. M. Star-Lack, J. A. Heanue, and M. S. Van Lysel, "Pilot study with a scanning-beam digital x-ray system," Am. J. Cardiol. **94**, 95E (2004).

[14]R. Sedgewick, *Algorithms in C*, 3rd ed. (Addison-Wesley, Reading, 1998).

[15]M. Vembar, M. J. Garcia, D. J. Heuscher, R. Haberl, D. Matthews, G. E. Bohme, and N. L. Greenberg, "A dynamic approach to identifying desired physiological phases for cardiac imaging using multislice spiral CT," Med. Phys. **30**, 1683–1693 (2003).

[16]M. A. Speidel, "Performance characteristics of the scanning-beam digital x-ray (SBDX) cardiac imaging system," Ph.D. dissertation, University of Wisconsin, 2003 (available from UMI Dissertation Services, University of Wisconsin, Ann Arbor, MI).

[17]J. M. Fitzpatrick, D. L. G. Hill, and C. R. Maurer, Jr., *Handbook of Medical Imaging Volume 2. Medical Image Processing and Analysis*, edited by M. Sonka and J. M. Fitzpatrick (SPIE, Bellingham, 2004), pp. 469–470.

[18]S. Bouix, K. Siddiqi, and A. Tannenbaum, "Flux driven fly throughs," in Proceedings of the 2003 IEEE Computer Society Conference on Computer Vision and Pattern Recognition, Vol. 1, pp. I449–I454, 2003 (unpublished); available at http://ieeexplore.ieee.org using the doi 10.1109/CVPR.2003.1211388.

[19]M. Brunet-Benkhoucha, F. Verhaegen, S. Lassalle, D. Beliveau-Nadeau, B. Reniers, D. Donath, D. Taussky, and J.-F. Carrier, "Clinical implementation of a digital tomosynthesis-based seed reconstruction algorithm for intraoperative postimplant dose evaluation in low dose rate prostate brachytherapy," Med. Phys. **36**, 5235–5244 (2009).

[20]L. Gepstein, G. Hayam, and S. A. Ben-Haim, "A novel method for nonfluoroscopic catheter-based electroanatomical mapping of the heart. In vitro and in vivo accuracy results," Circulation **95**, 1611–1622 (1997).

[21]A. P. Lowell and W. Sun, "Real-time x-ray tomosynthesis imaging using an ATCA general-purpose data acquisition and analysis platform," in IEEE Nuclear Science Symposium Conference Record, pp. 27–31, 2008 (unpublished); available at http://ieeexplore.ieee.org using the doi 10.1109/NSSMIC.2008.4775245.